# 5 Asteroid observations using the Spitzer Space Telescope

*The Spitzer Space Telescope (known as Space InfraRed Telescope Facility, SIRTF, until after launch) is the fourth and final member of NASA's series of space telescopes called* Great Observatories, *following the Hubble Space Telescope, the Compton Gamma Ray Observatory, and the Chandra X-Ray Observatory. Spitzer has imaging and spectroscopy capabilities in the mid-infrared wavelength range from 3.6–160 μm. Spitzer is the currently most sensitive mid-infrared telescope, owing mostly to its vantage point far away from the Earth atmosphere and thermal environment.*

*Spitzer was launched in 2003 and is expected to stay fully operational until spring 2009. Observing time with Spitzer is made available annually since summer 2004 through an international competition. We were awarded a total of four asteroid observing programs in open competition, two in cycle II (2005–06) and further two in cycle III (2006–07). As of 20 April 2006, i.e. up to Spitzer cycle III, there is a total of 16 asteroid observing programs with Spitzer, including our four.*[1]

*In sect. 5.1, some general information on Spitzer is provided, including its optical design. Sections 5.2 and 5.3 are devoted to the two focal plane instruments used in our observing programs, the InfraRed Array Camera (IRAC) and the InfraRed Spectrometer (IRS), respectively. In either section, the instrument capabilities are presented and our observing strategies and data reduction techniques are detailed. The scientific goals and achievements of our observations will be discussed in the following chapters.*

*More information can be found in the Spitzer Space Telescope Observer's Manual (referred to as SOM in the following) provided on-line by the Spitzer Science Center:* `http://ssc.spitzer.caltech.edu/documents/som/`. *See also Werner et al. (2004).*

[1] Awards of observing time for cycle IV were announced to successful proponents on 2 May 2007. We were awarded one cycle-IV program. Statistics is not yet publicly available.

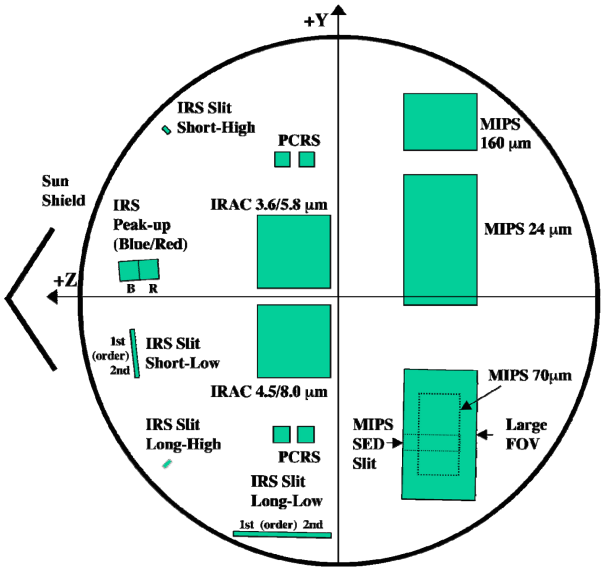


**Figure 5.1:** Aperture positions of the Spitzer science instruments on the focal plane. There are several apertures per instrument, corresponding to different instrument operation modes. Those for IRAC will be discussed in sect. 5.2, those for IRS in sect. 5.3 (MIPS is not used in our observations). Also on the focal plane are pointing control reference sensors (PCRS). The projected focal plane radius is 16′. (Fig. from SOM, p. 60).

## 5.1 Spitzer overview

The Spitzer spacecraft carries a 0.85 m reflecting telescope with three focal plane science instruments performing imaging and spectroscopy in the wavelength range from 3.6–160 μm. In flight, telescope and focal plane instruments are cryogenically cooled with liquid helium. The spacecraft was launched on a Delta rocket from Cape Canaveral, USA on 25 Aug 2003. Its orbit is heliocentric, trailing behind Earth, thus avoiding the adverse affects of the Earth atmosphere and thermal environment. After cooling down the telescope, followed by initial validation and calibration measurements, science observations began on 1 Dec 2003; they are expected to last as long as cryogen is available, probably until spring 2009.

The three science instruments are (see Fig. 5.1 for their position on the focal plane):

- **InfraRed Array Camera (IRAC)**, four imaging detectors operating at central wavelengths of 3.6, 4.5, 5.8, and 8.0 μm, respectively, each with a square field-of-view of about 5′ at a pixel scale of $\sim 1.2''$ (PI G.G. Fazio, Smithsonian Astrophysical Observatory, Harvard-Smithsonian Center for

Astrophysics);

- **InfraRed Spectrograph (IRS)**, a spectrometer covering the wavelength range from 5.2–38.0 µm at relative spectral resolutions $\lambda/\Delta\lambda$ between 64 and 128 (low-resolution mode) or 600 (high-resolution mode). IRS also has imaging capabilities at wavelengths of about 16 and 22 µm with a field of view of about $1' \times 1.2'$ at a pixel scale of $\sim 1.8''$ (PI J.R. Houck, Cornell University);

- **Multiband Imaging Photometer for Spitzer (MIPS)**, an imager with three broad-band filters centered at wavelengths of 24, 70, and 160 µm. MIPS has an additional low-resolution ($\lambda/\Delta\lambda \sim 20$) spectroscopy mode at wavelengths of 55–95 µm and a Total Power Mode for measuring the absolute sky brightness in that wavelength range (PI G. Rieke, Steward Observatory, University of Arizona). MIPS is not used in our observing programs and is thus disregarded in the following.

The spacecraft is operated by the Spitzer Science Center (SSC), located at the campus of the California Institute of Technology in Pasadena, CA, USA.

### 5.1.1 Spacecraft design and orbit

See Fig. 5.2 on p. 102 for an overview of the spacecraft design. Its main components are:

- Cryogenic Telescope Assembly: A cryostat attached to the helium tank; it contains the cold parts of the focal plane science instruments at a helium bath temperature of 1.4 K. The telescope itself is cooled through helium vapor vented off the cryostat to a temperature of 6–12 K.

- Spacecraft Bus, hosting all command and data handling units, along with the systems for attitude control and telecommunication. The spacecraft bus is not cooled, and thermally shielded from the cryogenic telescope assembly.

- Solar Panel and Solar Panel Shield, which provide electric power and at the same time shield the spacecraft (particularly the cryogenic assembly) from direct sunlight.

The permissible range of spacecraft attitude is severely constrained: The requirement to shield the spacecraft from direct sunlight virtually forbids “roll”

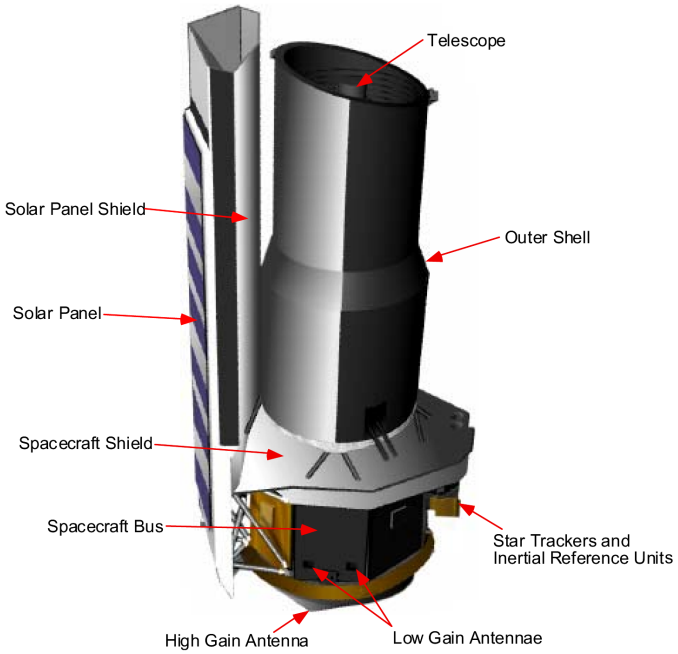


**Figure 5.2:** Design of the Spitzer spacecraft; it is $\sim 4$ m tall and $\sim 2$ m in diameter. The longest axis coincides with telescope boresight. (Fig. from SOM, p. 35).

rotations around telescope boresight (the roll angle is fixed to its nominal value $\pm 2°$). Furthermore, telescope pointing is restricted to solar elongations above 82.5° in order to prevent sunlight from entering the telescope, and to solar elongations below 120° in order to guarantee sufficient electric power output from the solar panels. Rotations about the axis pointing towards the Sun, however, are unconstrained, resulting in a viewing zone of annular shape, at solar elongations between 82.5 and 120°; see Fig. 5.3. This has a profound influence on observations of Solar System objects, which will be discussed in sect. 5.1.4.

Spitzer is on an Earth-trailing heliocentric orbit, drifting away from Earth at a rate of about 0.12 AU/yr. It is thus not only far away from the Earth atmosphere, but also from its thermal environment, which would otherwise substantially heat up the spacecraft and thus limit the cryogenic lifetime. Also, this orbit limits the projected size of the Earth and Moon avoidance zones for telescope observations.

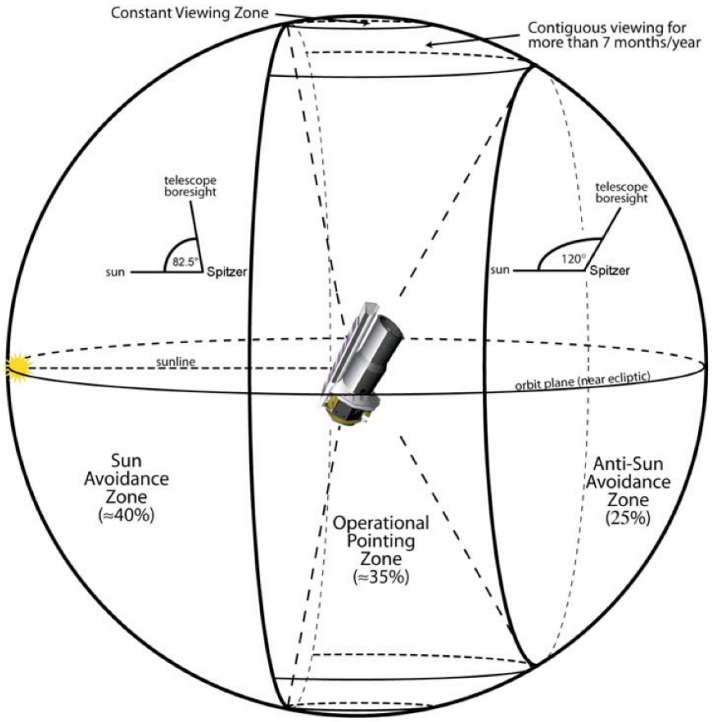


**Figure 5.3:** Depiction of the region into which Spitzer can point (Fig. from SOM, p. 26).

### 5.1.2 Optical design

The telescope has an aperture of 0.85 m and a focal ratio of $f/12$ (at 5.5 K; focal length 10.2 m) and follows the Ritchey-Chrétien variant of the Cassegrain design. It is entirely made of beryllium, a light metal of low heat capacity at low temperatures. Imaging is diffraction limited at wavelengths above 5.5 µm.

There are no moving parts on the spacecraft, with the exception of the camera shutter of IRAC (which is, however, not being planned to be used in flight) and a mirror inside MIPS. The absence of (movable) camera shutters hampers calibration measurements, in particular dark current measurements, which will be discussed in the appropriate instrument sections.

Only one science instrument is powered up at any time, in order to minimize cryogen consumption due to dissipation of electric power. Instrument change-over entails a substantial amount of engineering and calibration activities. Instruments usually stay on for roughly one week, called an instrument campaign.

Spitzer has different mechanisms for changing and controlling telescope pointing which, in the absence of moving parts, is tantamount to spacecraft attitude. The

accuracy of "blind" slews is $0.5''$ ($1\sigma$), which is sufficient to acquire imaging targets but not always sufficient for spectroscopy. Relative pointing (for slews of up to $30'$) is more accurate. Pointing is stable to within $0.1''$ ($1\sigma$) over 1000 s. Spitzer is capable of linearly tracking moving targets of apparent velocities of up to $1''$/s, which is sufficient for all our programs.

### 5.1.3 Planning and proposing observations

The majority of Spitzer observing time is open to international observers in an open competition. General Observer (GO) proposals are invited by the Spitzer Science Center (SSC) on an annual basis in mid February, programs awarded observing time are scheduled within a 12-month period starting the following summer. Director's Discretionary Time (DDT) is available for observations of unexpected phenomena of particularly high scientific merit which cannot be accommodated by GO programs. DDT can be applied for at any time on relatively short notice. Three out of our four Spitzer programs were GO programs, we were awarded DDT for one program.

All proposals must be submitted electronically to the SSC, along with a full specification of all proposed observations, using the SSC-supplied software SPOT (Spitzer Planning Observations Tool). SPOT can be used to determine times at which prospective targets are observable with Spitzer; Spitzer pointing is constrained in solar elongation (see sect. 5.1.1), neither may the telescope be pointed close to bright moving sources (planets, dwarf planets, the Moon, and the brightest asteroids) which may temporarily damage the detectors.

In SPOT, different types of constraints can be imposed on the relative or absolute timing of proposed observations, we will discuss some of these in sect. 5.1.4. Any timing constraint imposed must be given a scientific justification.

If an observing program is accepted, the parameters entered into SPOT are automatically transformed into commands uplinked to the spacecraft.

Due to Spitzer's high sensitivity and accuracy, in the planning of observations effects must be considered which are unfamiliar from ground-based mid-infrared observations. For example, contamination due to faint background sources becomes a problem (see sect. 5.1.4), potentially leading to confusion noise. Furthermore, possible detector dysfunctionalities (e.g. due to cosmic ray hits or defective pixels) together with the non-interactive nature of Spitzer observations require imaging observations to be highly dithered, i.e. several consecutive observations of the target should be taken at small spatial offsets from one another. SPOT pro-

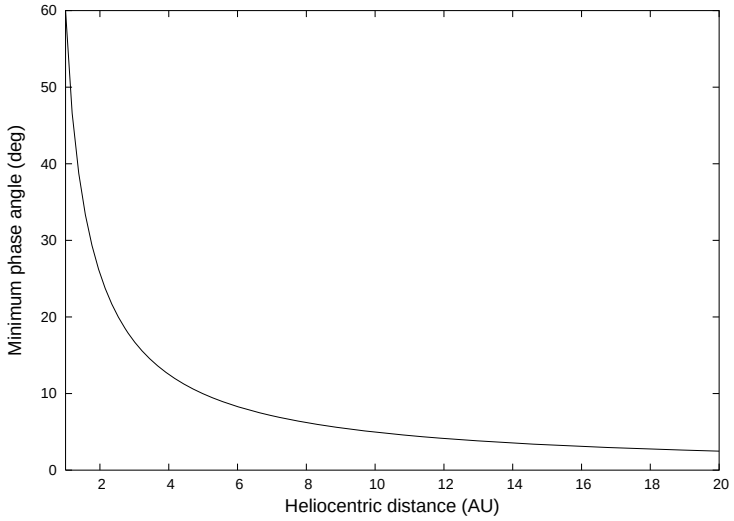


**Figure 5.4:** Minimum solar phase angle, $\alpha_{\min}$ for Spitzer observations of Solar System objects as a function of heliocentric distance, $r$ (see eqn. 5.1). Spitzer's heliocentric distance $r_{\mathrm{SST}}$ is assumed to equal 1 AU.

vides several instrument-specific templates for that. Dithering has the additional advantage of mitigating against any residual pixel-to-pixel variations in sensitivity not caught in the flat-fielding process.

### 5.1.4 Asteroid-specific aspects to observation planning

**Parallax** Spitzer is *not* on a geocentric orbit, but trails behind the Earth on a heliocentric orbit at a steadily increasing geocentric distance. This causes a parallax between the Spitzer-centric and geocentric apparent positions of solar-system targets, particularly for near-Earth objects. *Horizons,* the JPL on-line ephemeris service (`http://ssd.jpl.nasa.gov/?horizons`), can be used to generate Spitzer-centered ephemerides of solar-system objects—the telescope code for Spitzer is −79.

**Solar elongation constraints** As discussed in sect. 5.1.1, spacecraft design constrains telescope pointings to solar elongations between 82.5 and 120°. While for inertial targets this only constrains the *time* of their observability, for solar-system objects this prevents observations close to opposition (solar elongation of 180°), where it would be preferable to observe them. Not only do solar-system objects generally reach their peak brightness at opposition, but they are also best observable from ground during that time. The impossibility of close-to-opposition

Spitzer observations thus hampers simultaneous ground-based support observations with, e.g., optical telescopes, which would have been advantageous for some of our programs. Most importantly, however, the solar elongation constraint provides a lower limit on the solar phase angle, $\alpha$, at which objects are observable—minimum phase angles occur at opposition. The importance of the phase angle for thermal modeling is discussed in sect. 2.2.5. The minimum solar phase angle $\alpha_{\min}$ for Spitzer observations of solar-system objects is a function of their heliocentric distance $r$ and of Spitzer's heliocentric distance $r_{\mathrm{SST}}$:

$$\alpha_{\min}(r) = \arcsin \frac{\sqrt{3}}{2} \frac{r_{\mathrm{SST}}}{r}, \tag{5.1}$$

where it is assumed that the minimum phase angle occurs at an elongation of 120° (true for $r > r_{\mathrm{SST}}$). See Fig. 5.4 on p. 105 for a plot.

**Instrument change-over** Only one Spitzer instrument is powered up at any time. Therefore, multi-wavelength observations using different instruments entail a time gap between observations of a few hours at least, which may result in an additional flux uncertainty due to lightcurve effects.

**Background sources** With ground-based mid-infrared telescopes such as the IRTF (see chapter 4), only very bright targets can be observed, which are virtually guaranteed to be the only observable source inside the FOV. This is different with Spitzer. Its high sensitivity leads to several potential problems, which need to be mitigated against in both observation planning and data analysis:

- Very bright background sources inside (or close to) the FOV heavily saturate the detector and compromise observations due to, e.g., blooming. The timing of asteroid observations must therefore be constrained to times where no such bright background source is near-by. This time-consuming task can be accomplished by overlaying star charts with the asteroid path using SPOT (see, e.g., Fig. 5.5 on p. 109). The most useful star charts for this purpose are those derived from the IRAS survey at wavelengths of 12 and 25 µm. Most IRAS sources would heavily saturate Spitzer cameras in deep integrations.

- For deep imaging observations, the brightness of (spatially resolved or unresolved) background sources may be comparable to that of the asteroid target, causing difficulties for reliable target flux extraction in their vicinity.

Although this latter effect is mitigated by the apparent motion of asteroids, it severely compromised several of our asteroid observations. Note that deep imaging observations regularly consist of a time series of individual pointings, during which the asteroid moves. Data can be partially recovered by rejecting frames with close asteroid-star encounters.

Other reasons for imposing timing constraints on asteroid observations may be target brightness (particularly for near-Earth objects, where brightness is a strong function of time) or phased observations of the asteroid lightcurve.

### 5.1.5 Spitzer data reduction

The SSC discourages observers from performing calibration observations; instead, calibration observations are regularly performed by members of the instrument teams along with maintenance operations. All science data are partially reduced at the SSC. To this end, the SSC hosts instrument-specific sets of automated partial data reduction routines, referred to as the *BCD pipelines,* where BCD stands for Basic Calibrated Data. The BCD pipelines remove most known instrument artefacts from the data and also perform absolute flux calibration. While raw data are made available to the observer, most parts of the BCD pipelines and most required calibration files are not.

The remaining data reduction steps to be taken by the observer include removal of residual instrument artefacts, stacking and coadding appropriate data subsets, extraction of target fluxes, and correction of target fluxes for, e.g., the effect of filter breadth. See the appropriate subsections of sect. 5.2 and 5.3.

## 5.2 InfraRed Array Camera (IRAC)

IRAC (acronym for InfraRed Array Camera) is an imaging camera at the low-wavelength end of Spitzer's spectral coverage: It consists of four detectors operating at central wavelengths around 3.6, 4.5, 5.8, and 8.0 µm (referred to as channels 1–4 in the following). Each detector has a square field-of-view (FOV) 256 pixels wide, corresponding to roughly $5.2'$ at a pixel scale around $1.2''$.

At IRAC wavelengths, reflected sunlight and thermal emission contribute to the observable asteroid flux. At 3.6 µm (channel 1), thermal flux is generally negligible relative to reflected sunlight, the converse applies to channel 4 (8.0 µm). The IRAC wavelength range is at the Rayleigh-Jeans tail of the emission of stellar back-

**Table 5.1:** IRAC filter wavelengths and spectral breadths. See eqn. 5.7 on p. 123 for a definition of the effective wavelength.

| | Channel 1 | Channel 2 | Channel 3 | Channel 4 |
|---|---|---|---|---|
| Mnemonic wavelength (µm) | 3.6 | 4.5 | 5.8 | 8.0 |
| Effective wavelength (µm) | 3.550 | 4.493 | 5.731 | 7.872 |
| FWHM (µm) | 0.74 | 1.02 | 1.41 | 2.88 |
| Relative filter width | 21% | 23% | 25% | 36% |

ground sources, therefore their brightness relative to that of asteroids decreases with wavelength.

This section starts with a short overview of the instrument layout and its capabilities as used in our observing programs (sect. 5.2.1). Our asteroid observation strategies are described in sect. 5.2.2. In the following two sections, we describe the employed data reduction techniques: First the partial, automated IRAC BCD pipeline hosted by the Spitzer Science Center (sect. 5.2.3), then the data reduction techniques employed by us (sect. 5.2.4). Sect. 5.2.5 is devoted to tests of our data reduction pipeline.

More information on instrument layout and nominal data quality can be found in Fazio et al. (2004), Hora et al. (2004), and in the IRAC data handbook provided on-line (Spitzer Science Center, 2006a) (we made use of version 3.0 from 20 Jan. 2006, `http://ssc.spitzer.caltech.edu/irac/dh/`).

### 5.2.1 Instrument layout

IRAC consists of four CCD detectors sharing a common electronic and cryogenic framework. Channels 1 and 2 are In:Sb detectors, channels 3 and 4 are Si:As detectors. Filter wavelengths and spectral breadths for all channels are summarized in table 5.1. The detectors are situated inside the Cryogenic Telescope Assembly (see Fig. 5.2 on p. 102) at a helium bath temperature of 1.4 K. All instrument control units are in the Spacecraft Bus. Each detector is 256 x 256 pixels in size, with a projected pixel size around $1.2''$ x $1.2''$. Each field of view (FOV) is about $5.2'$ x $5.2'$ wide. Channels 1 and 3 share a common aperture and FOV using a dichroic beam-splitter, the same applies to channels 2 and 4. The edges of the two FOVs are separated by about $1.5'$, so there is no overlap on the sky (see Fig. 5.5).

IRAC imaging is limited by diffraction with mean diffraction widths of $1.66''$, $1.72''$, $1.88''$, and $1.98''$ (FWHM) for channels 1–4, resp. With a $\sim 1.2''$ pixel scale,

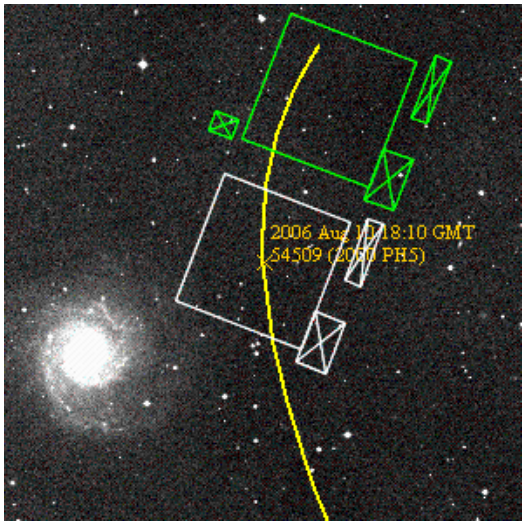


**Figure 5.5:** Projection of the two IRAC FOVs onto the sky: The FOV shared by channels 2 and 4 is depicted white, that of channels 1 and 3 is green. The crossed-out rectangles next to the FOVs represent the respective straylight-avoidance zones (see text). Depicted is a $20' \times 20'$ patch of Digital Sky Survey (DSS) data centered at the position of (54509) YORP (then known under its provisional designation 2000 PH5) on 10 Aug 2006, 18:10 UT (yellow line and cross). The large spiral galaxy is Messier object 74 = NGC 628.

the four IRAC point-spread functions are undersampled.

In standard observing mode, there are four selectable options for the integration time per image frame (frame time) ranging from 2–100 s, see table 5.2 on p. 110 for the corresponding sensitivities and table 5.3 for the saturation limits. IRAC observations typically consist of a series of $n$ consecutive frames, which are later stacked; the total signal-to-noise ratio $S/N$ for a source with flux $f$ then equals

$$S/N(f) = \frac{f}{s}\sqrt{n} \tag{5.2}$$

where $s$ denotes the single-frame sensitivity $s$ as in table 5.2. For deep IRAC observations, the dominant source of uncertainty is celestial background radiation due to the emission and scattering of sunlight by zodiacal dust. The zodiacal dust is concentrated in the ecliptic plane, therefore IRAC's sensitivity is a strong function of ecliptic latitude. We planned all observations assuming high background, as is appropriate for most Solar-System objects.

IRAC is continuously exposed to the sky; there is a shutter, which was used for laboratory measurements on ground, but it is not operated in flight in order to avoid any operational risk imposed by this moving part. Therefore, all

**Table 5.2:** IRAC point-source sensitivity ($1\sigma$ in units of µJy; see also eqn. 5.2 on p. 109) for one image frame of the stated integration time (frame time). The celestial background is assumed to be high, as is appropriate for most asteroid observations. Long exposures in channel 4 are background-limited; "100 s" frames in channel 4 are automatically converted into 2 frames of 50 s each.

| Frame time (sec) | 3.6 µm | 4.5 µm | 5.8 µm | 8.0 µm |
|---|---|---|---|---|
| 100 | 1.3 | 2.1 | 14 | 18 |
| 30 | 2.5 | 4.1 | 27 | 32 |
| 12 | 4.8 | 7.1 | 44 | 52 |
| 2 | 34 | 41 | 180 | 156 |

**Table 5.3:** Largest non-saturated point-source flux for the four IRAC channels and the stated frame times. Units in this table are mJy, *not* µJy as in table 5.2! High celestial background is assumed.

| Frame time (sec) | 3.6 µm | 4.5 µm | 5.8 µm | 8.0 µm |
|---|---|---|---|---|
| 100 | 3.8 | 3.9 | 27 | 28 |
| 30 | 13 | 13 | 92 | 48 |
| 12 | 32 | 33 | 230 | 120 |
| 2 | 190 | 200 | 1400 | 740 |

four detectors take science quality data simultaneously. Even if only one channel is requested, the same field is observed in a second channel, while an adjacent ("serendipitous") field is observed in the two remaining channels; for some purposes, we found it useful to obtain observations in one FOV by requesting observations of a suitably offset field with the other FOV (see sect. 5.2.2.c). Data from all four channels are processed through the BCD pipeline and made available to the observer.

IRAC is offset from the optical axis of the Spitzer focal plane (see Fig. 5.1 on p. 100) leading to optical distortion, i.e. the projected shape and size of pixels vary across the detector. The distortion has been modeled by the Spitzer Science Center to an accuracy of $0.1''$ and must be corrected for in order to avoid significant photometric errors.

For all four IRAC channels, a certain amount of stray light is scattered onto the detectors. This is only critical if bright background sources are in certain "stray light avoidance zones" close to the FOV (see Fig. 5.5 on p. 109).

### 5.2.2 Observing strategy for asteroid photometry

IRAC observations have to be designed in a way quite different from ground-based mid-infrared observations:

- Observation design must be very robust because Spitzer executes all observations autonomously, without the possibility of real-time observer interaction. Also, the exact time at which observations are carried out is usually unknown at the planning stage—absolute timing constraints can be imposed by the observer but require a scientific justification. Once an observation is scheduled (roughly 2–5 weeks in advance), no more changes to the observation parameters can be made.

- Observations of faint targets are plagued by background sources of comparable brightness, the abundance of which grows rapidly with observation depth. While in the case of MIRSI, suitable targets are practically guaranteed to be the only observable source inside the FOV, IRAC observations must be designed in a way that mitigates against background contamination.

- There is also a non-negligible number of heavily saturating sources which, if inside the FOV, spoil the entire image frame and potentially subsequent image frames through latent effects. These must be prevented from entering the FOV.

IRAC observations are defined in the Spitzer Proposal Tool SPOT by specifying a target, the desired IRAC channels, the integration time per image frame, and the total number of image frames per channel to be taken. There are two options, which can be combined, for choosing the number of image frames: Dithering telescope boresight a user-defined number of times around the target location or identical in-place repeats. While dithering causes a small overhead for telescope slewing and settling, it enhances the accuracy and robustness of observations by mitigating against small-scale detector defects (e.g. permanently defective pixels or cosmic ray hits) and any residual pixel-to-pixel variations in sensitivity.

The timing of observations can be constrained by the observer in several ways, but it is stipulated in the Call for Proposals that they be minimized. Timing constraints require a compelling scientific justification, otherwise a lower priority will be assigned to the program by both the Time Allocation Committee and, if the program is accepted, in the scheduling queue.

#### 5.2.2.a Integration time

We determined the required total integration time from eqn. 5.2 on p. 109, depending on expected target flux and on our predefined goal for the total $S/N$ required to reach our scientific goals.

The expected flux of our asteroid targets at IRAC wavelengths depends on several, generally unknown, asteroid parameters such as diameter and apparent color temperature. This may induce a flux uncertainty of up to a factor of 10. The exact time of observations is not known at the planning stage, adding to the flux uncertainty.

For each target, we calculated upper and lower flux limits assuming appropriate end-members of the plausible range of physical properties and ephemerides. We requested conservatively deep integrations, such that we would barely reach our $S/N$-goal assuming the lower flux limit. We also checked against the appropriate IRAC saturation limits (see table 5.3 on p. 110).

#### 5.2.2.b Timing constraints

We generally had to prevent Spitzer from observing at undue times by imposing absolute timing constraints, i.e. by explicitly specifying times during which the observations should take place.

For all asteroid targets, we identified "avoidance times" during which the target path is close to bright known infrared sources, which would heavily saturate the detectors and potentially lead to temporary detector damage if they enter a FOV or a straylight avoidance zone. This was done by overlaying star charts resulting from the IRAS 12 µm survey with the projection of the IRAC FOVs and the Spitzer-centric asteroid path (note the parallax between Spitzer and Earth) throughout the times of Spitzer observability; see Fig. 5.6 for a typical example. To be sure, we considered every known IRAS source to be potentially damaging IRAC, due to its much higher sensitivity. Since heavy detector saturation may compromise subsequent observations through persistent latent images, we also kept the off-target FOV clear of IRAS sources.

Generally, this resulted in very mild timing constraints, typically barring a few hours per week, a notable exception being times during which the asteroid path intersects regions of high background source density, e.g. at low galactic latitudes.

For NEA targets, we additionally disabled observing at times when the target was too distant and thus too faint for successful observing.

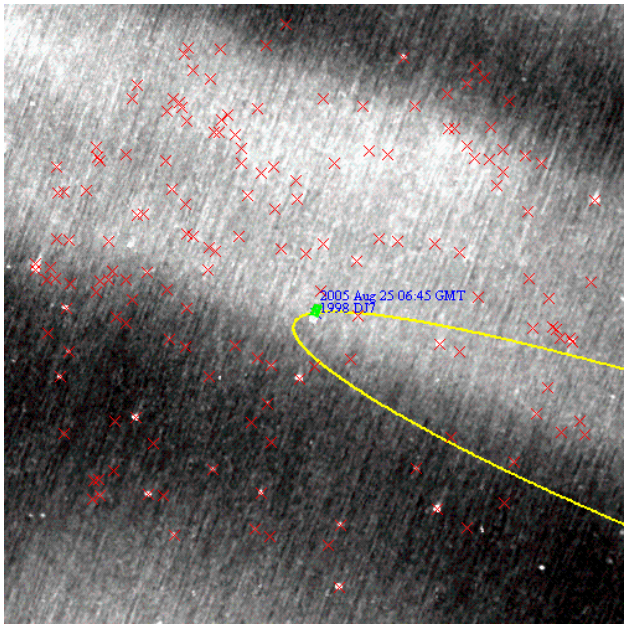


**Figure 5.6:** Star chart (12.5° × 12.5°) derived from the IRAS 12 µm survey, overlaid with the Spitzer-centric path of asteroid (33143) 1998 DJ7 (yellow line), known IRAS sources (red crosses) and the two IRAC FOVs (green and white as in Fig. 5.5 on p. 109, but note the size difference!).

#### 5.2.2.c Dithering

For most of our observations, telescope boresight is slightly altered between consecutive observations, such that the on-chip position of the target *dithers* around the FOV center. While this causes a slight overhead for telescope reorientation and settling, it helps mitigate against the effects of defective pixels or residual pixel-to-pixel variations in sensitivity.

SPOT provides several standard dither patterns. As recommended by the SSC, we generally chose mid-scale dither patterns, which keep our target on chip at all times. We generally chose the longest possible frame time (100 s) and the required number of dither positions to reach the total integration time previously determined (see sect. 5.2.2.a). We always used five or more dither positions, however, and therefore reduced the frame time for shallow observations.

For most deep IRAC observations, we employed a non-standard dither pattern in order to mitigate more efficiently against contamination from celestial background sources. For deep IRAC observations, practically no field in the sky is guaranteed to be clear of potentially interfering background sources, so it is impractical to avoid them by imposing timing constraints. Furthermore, unresolved

faint background sources (or diffuse but structured emission, e.g. from zodiacal emission or galactic cirrus) decrease the accuracy at which photometry can be performed, leading to confusion noise which may limit the accuracy of deep IRAC observations.

This is mitigated against by the apparent movement of our targets: If the target moves by more than one PSF width between the first and last image in a series, then frames with background sources close to the asteroid path can be rejected (see sect. 5.2.4.a). Also, background structure is reduced by coadding image frames with different asteroid positions relative to the inertial background (see sect. 5.2.4.c).

To this end, we have designed deep asteroid observations in a highly redundant way, consisting of up to 144 on-target image frames per observation. In order to maximize the time baseline and thus the apparent asteroid motion between first and last frames, we have used a non-standard dither pattern. As opposed to the standard IRAC dither patterns, where the FOV shared by channels 2 and 4 is on target for the first half of the time, followed by the FOV of channels 1 and 3, we had the FOVs "take turns" on target up to ten times. This nearly doubled the temporal baseline at the expense of a small overhead for the additional telescope slews.

SPOT does not provide such dither patterns. We implemented them in an indirect way taking advantage of the IRAC peculiarity that even if only one channel is requested, all channels are exposed to the sky and read out, and all data are processed in the BCD pipeline. We requested a "moving cluster target" to be observed by channels 2 and 4, such that odd-number cluster positions are on target (not offset) and even-number cluster positions are offset by $402''$ along the row axis in IRAC array coordinates, centering the 2nd FOV on target. Typically, a standard dither pattern is performed on each cluster position.

### 5.2.3 IRAC BCD pipeline

As for all Spitzer science data, IRAC data are partially reduced and calibrated at the SSC using an automated set of computer routines called the IRAC BCD pipeline (see sect. 5.1.5). It outputs one BCD file per pointing and detector, i.e. an image file in FITS format.

In this section, those aspects of the IRAC BCD pipeline which are relevant to our programs shall be sketched. The reference for most of the material presented here is the IRAC pipeline description document (Spitzer Science Center, 2005a).

#### 5.2.3.a Correction for dark current

An integration-time dependent dark-current estimate is subtracted from all images in the BCD pipeline. The detector dark-current levels for all possible integration times were determined on ground. In orbit, the absolute dark-current level cannot be measured since the shutter is not moved (see above). However, drifts in dark-current level are monitored based on sky dark frames, which are obtained from frequent, highly dithered observations of sky regions of very low emission (very low zodiacal background, only few bright sources such as stars).

#### 5.2.3.b First-frame effect

For an unknown reason, the dark-current level is a function of the time elapsed since the end of the previous detector readout, the so-called first-frame effect. This adds an unpredictable offset, chiefly to the first few frames in a series of observations. In order to mitigate against the first-frame effect, one or two redundant observing frames of short integration time are added by default at the beginning of each series of observations. The remaining background-level uncertainty is not corrected for in the BCD pipeline and must be considered in the data reduction, cf. sect. 5.2.4.b.

#### 5.2.3.c Flat-fielding

To correct for the pixel-to-pixel variation in sensitivity, IRAC science data are divided by a gain map over the FOV normalized to one, called a flat field. It is determined from frequent, highly dithered observations of predefined regions of high zodiacal emission (which is spatially relatively constant over the IRAC FOV; note again that IRAC's shutter is not used in flight) and only small numbers of stars or galaxies. The images frames obtained are cleaned from localized sources and cosmic ray hits, then coadded and normalized to a median of one.

The flat-field frames thus obtained were seen to be constant within the observational uncertainty over the first two years of Spitzer operations.

#### 5.2.3.d Flux calibration

Flux calibration factors were determined from observations of a set of calibration stars before the beginning of normal science operations and are confirmed by regular reobservations (Reach et al., 2005). The absolute calibration accuracy is

estimated to be within 3 %, limited by the uncertainty in calibration star flux. The relative accuracy (temporal stability) of IRAC is 1.5 % (rms) over a year.

Calibration-star data-counts are obtained via synthetic aperture photometry using a particular set of aperture and sky-annulus radii (aperture radius: 10 pixels, annulus radii: 10 and 20 pixels); IRAC data should be reduced using the same parameters.

For the reduction of most deep observations these parameters are impractical. Smaller aperture and sky annulus radii can be used, but flux values thus obtained require a so-called aperture correction to be applied (see sect. 5.2.4.f).

The calibration procedure assumes targets to be point-like; this is a safe assumption for our asteroid targets, since their angular size is well below the IRAC diffraction widths.

IRAC is a broad-band photometer (see table 5.1 on p. 108). In order to convert the passband-integrated detector response into monochromatic flux values at the effective filter wavelengths, assumptions must be made on the target spectrum. BCD fluxes are corrected for a spectrum inversely proportional to wavelength. Different target spectra require color corrections to be made, which can be significant in the case of asteroids (see sect. 5.2.4.g).

Calibrated images are in units of flux per solid angle. Note that this is *not* equivalent to flux per pixel due to distortion (see above).

#### 5.2.3.e Pointing refinement

Spitzer's nominal pointing accuracy is $0.5''$, less than half the width of an IRAC pixel. The astrometric accuracy of taken image frames is further refined to an accuracy of $0.15''$ by matching the positions of detected sources with star catalogs (usually the 2 Micron All Sky Survey, 2MASS), more than sufficient for our needs.

### 5.2.4 Data reduction steps taken by us

We start our data reduction efforts at the BCD stage. First, unusable or irrelevant (off-target) BCD frames are filtered out. This includes visual inspection of all image frames (see sect. 5.2.4.a).

Then, the remaining BCD files belonging to one observation are coadded to a mosaic image in the asteroid rest frame. This includes several image manipulation tasks in order to mitigate against celestial background structure and to remove further detector effects and transient artefacts such as cosmic ray hits. These are

described in sections 5.2.4.b and 5.2.4.c.

Asteroid fluxes are determined from the mosaic images. This includes several corrections for known detector or source properties (see sections 5.2.4.d through 5.2.4.g).

All IRAC BCD files considered in this thesis were produced by the BCD pipeline version 14. For mosaicking, the software package MOPEX was used. MOPEX is provided by the SSC (`http://ssc.spitzer.caltech.edu/postbcd/download-mopex.html`; we used the version for Linux named 030106, released on 1 March 2006).

#### 5.2.4.a Filtering frames

Image frames that were irrelevant or unusable for our purposes were rejected from further analysis after visual inspection.

Due to IRAC's design with two non-overlapping fields-of-view (see Fig. 5.5 on p. 109) constantly exposed to the sky, the fields-of-view "take turns" on the target in a user-defined way when observing a point source in all four channels. Therefore, half of the downloaded image frames are off target and irrelevant for our purposes. Those were deleted, which significantly saved on storage space—and on computer time during sub-sequent analyses.[2]

Also, as introduced in sect. 5.2.3.b, each series of IRAC observations starts with one or two redundant integrations of reduced integration time in order to mitigate against the first-frame effect. Those images were deleted.

We visually inspected each remaining image frame before further analysis in order to reject unusable frames. Those include frames with very bright on-chip sources (or particularly bad cosmic ray hits) compromising the image quality throughout the detector through blooming effects. Also frames with detector artefacts, cosmic ray hits, or background sources within a few pixels from the target location were rejected. Generally, only parts of the data were affected due to dithering and the apparent movement of the asteroid target relative to the fixed star background.

#### 5.2.4.b Background matching

The first-frame effect (sect. 5.2.3.b) is a drift of the background levels in a series of observations, causing difficulties for outlier rejection during mosaicking (cf. sect. 5.2.4.c). First frames in a series are most affected.

[2] Note that a single deep IRAC observation can easily result in several hundred megabytes of data.

Although the first frame is always rejected (see above), it is nevertheless required to match the background levels of image frames to be mosaicked. This is accomplished using the program *overlap.pl,* which is part of the MOPEX package. It determines an offset value to each input image such that the pixel-by-pixel difference between overlapping areas of pairs of input images is minimized.

In a first step, the program reprojects and interpolates the BCDs onto a common rectangular grid. In a second step, bright sources above a user-specified detection threshold, particularly cosmic ray hits, which would bias the overlap correction, are masked and excluded from further processing. Then the additive overlap corrections are calculated and the corrected images are saved.

The detection threshold for bright object masking must be adjusted on a case-by-case basis, after evaluation of the mosaicking process.

#### 5.2.4.c Mosaicking and outlier rejection

Generally, IRAC observations are not performed as a single frame of the required integration time, but rather as a set of at least 5 correspondingly shorter integrations (our deepest IRAC observation consists of 144 individual BCD frames). Usually, telescope boresight of the individual observations is slightly altered between consecutive observations, such that the on-chip position of the target dithers around the FOV center (see sect. 5.2.2). Deriving target fluxes thus requires combining these exposures into a single high signal-to-noise image, referred to as mosaic.

Mosaicking is the most time-consuming part of IRAC data reduction, both in terms of computer time and number of iterations generally required to achieve a satisfactory result. We use the program *mosaic.pl,* part of the software package MOPEX, for this task. Mosaicking is done in three consecutive steps:

**Reprojection** Image data are reprojected and interpolated onto a common rectangular grid with a pixel scale of $1.20''$.[3] In particular, the effects of optical distortion are taken into account.

The asteroid rest frame is used as reference frame, i.e. the asteroid position is constant on all reprojected images while the positions of inertial background sources vary. In some of our observations, background star trails are longer than $10''$.

[3] IRAC flux calibration is tied to a pixel scale of $1.22''$. See sect. 5.2.5 for a discussion.

**Outlier rejection** Outlier pixels containing anomalously high or low signal are detected and rejected. These may be due to cosmic ray hits or detector artefacts, which may be permanently bad pixels or in response to a previous over-exposure, e.g. due to a cosmic ray hit (see Spitzer Science Center, 2006a). Also non-co-moving sources are partially rejected.

Outlier detection is based on pixel-wise image-to-image comparison. MOPEX provides three complementary algorithms for that; careful parameter tuning on a case-by-case basis is required in order to reliably reject outliers while keeping legitimate sources. It is crucial to inspect the maps of rejected pixels and to visually compare them with the input images in order to gage the quality of outlier rejection—the Airy rings around targets, in particular, are in danger of being erroneously rejected. Several reiterations may be required. If background matching was not well performed (see sect. 5.2.4.b), large parts of one input image may be flagged as outliers, requiring a reiteration of that step, too.

**Coaddition** A mosaic is generated by pixel-wise averaging those parts of the input images flagged as good. Also a coverage map is generated, indicating the number of good input image pixels used for each output pixel. Coverage maps are particularly useful for gaging the quality of mosaics.

#### 5.2.4.d Automated source extraction and photometry using MOPEX

MOPEX contains a program to automatically determine the position and absolutely calibrated brightness of point sources called APEX. APEX fits segments of mosaic images with the point-spread function, which is constant over time to a high accuracy. If a satisfactory fit is reached, APEX assumes a detection and determines the source flux by scaling the point-spread function and (if requested by the user) fitting the background.

Using APEX for flux determination is not generally recommended by the SSC (since flux calibration is performed using synthetic aperture photometry), but considered preferable inside fields containing many point sources: In the case of two or more sources whose point-spread functions overlap significantly, synthetic aperture is futile, whereas point-spread-function fitting still has a certain chance of success.

While we could determine flux values of calibration standard stars using APEX (c.f. sect. 5.2.5), we got no meaningful results in the case of asteroids with near-by stellar sources. We reckon the reason for this is the movement of the asteroid

targets relative to the inertial background: While on mosaic images the point-spread function is probably a good match to the image of the asteroid itself, the trails of background stars are only poorly matched.

#### 5.2.4.e Synthetic aperture photometry

Instead, we extracted asteroid flux densities from mosaicked images using the synthetic aperture photometry routines used for the analysis of IRTF data (see sect. 4.4.1.a; the software has been developed by M. Delbo', 2004). We generally used different combinations of aperture and sky annulus radii for which aperture correction factors were available (see sect. 5.2.4.f). Structure in the celestial background (e.g. background stars) often necessitated using small radii for both aperture and sky annulus. This effect is more severe in the short-wavelength channels 1 and 2 (the relative brightness of asteroids is larger in channels 3 and 4).

Before extracting fluxes, we converted the units of mosaic images from MJy/sr into µJy/pixel, such that the photometry output is in units of µJy.

#### 5.2.4.f Aperture correction

Let $f_{i,j,k}$ denote the flux contained in an aperture of radius $i$ minus the sky background content estimated from the flux inside an annulus of inner radius $j$ and outer radius $k$ (all radii in pixels). In general, $f_{i,j,k}$ is a function of $i$, $j$, and $k$: Varying $i$ changes the percentage of the point-spread function (PSF) energy content contained in the aperture, small values for $j$ and $k$ imply that parts of the source flux are inside the sky annulus, leading to sky-background overestimation and hence flux underestimation.

By virtue of the IRAC flux calibration scheme (see sect. 5.2.3.d), $f_{10,10,20}$ is generally the best available approximation to the "true" flux $f_{\mathrm{true}}$. Structure in the celestial background, however, often renders it impractical to use such large radii (see above). Fortunately, due to the high temporal stability of the IRAC PSFs, the ratio $f_{10,10,20}/f_{i,j,k}$ is very stable, such that smaller radii can safely be used if the resulting flux is later multiplied by the appropriate *aperture correction factor* $AC_{i,j,k}$:

$$f_{10,10,20} \sim AC_{i,j,k} f_{i,j,k}. \tag{5.3}$$

Aperture correction factors are obviously dependent on the pixel scale. Those quoted in the IRAC datahandbook (p. 53) are for a pixel scale around 1.22″ and therefore not directly applicable to us, since we use a mosaic pixel scale of 1.20″.

**Table 5.4:** Aperture correction factors $AC_{i,j,k}$ for the four IRAC channels and different aperture and sky annulus radii $i$, $j$, and $k$ (in mosaic pixels, 1.20″ each), see eqn. 5.3. The values in this table are assumed to be accurate to roughly one percent and differ slightly (but significantly) from those given in the IRAC data handbook (p. 53) due to the different pixel sizes used (see sect. 5.2.5).

| Aperture | Sky annulus | Channel 1 | Channel 2 | Channel 3 | Channel 4 |
|---|---|---|---|---|---|
| 2 | 2–6 | 1.253 | 1.278 | 1.414 | 1.615 |
| 2 | 10–20 | 1.236 | 1.259 | 1.393 | 1.582 |
| 3 | 3–6 | 1.128 | 1.133 | 1.154 | 1.255 |
| 3 | 10–20 | 1.110 | 1.114 | 1.131 | 1.235 |
| 5 | 5–10 | 1.057 | 1.067 | 1.065 | 1.081 |
| 5 | 10–20 | 1.043 | 1.049 | 1.050 | 1.060 |
| 10 | 10–20 | 1.000 | 1.000 | 1.000 | 1.000 |

We have therefore determined aperture correction factors to be used with our mosaic pixel scale of 1.20″ from observations of the bright star HD 165459, which is also used as an IRAC photometric calibration standard (see also sect. 5.2.5). See table 5.4 for our results, which we estimate to be accurate to roughly one percent, limited by the statistical uncertainty of the star flux determinations.

Note that this procedure can only be used in the case of a high temporal PSF stability—it cannot be used for, e.g., mid-infrared asteroid imaging using the IRTF (where the PSF depends on variable parameters such as seeing or telescope focus).

#### 5.2.4.g Color correction

IRAC is a broad-band photometer. Derivation of monochromatic flux values from the detector output therefore requires assumptions on the target spectrum to be made and an appropriate choice of the effective filter wavelength $\lambda_0$. Flux values obtained so far are correct for a nominal source spectrum $f_{nom}(\lambda) \propto \lambda^{-1}$ (with wavelength $\lambda$) (see sect. 5.2.3.d). For other target spectra, this causes a systematic multiplicative offset, requiring a *color correction* to be made. Color correction factors for several target spectra are tabulated in the IRAC data handbook, p. 48 (Spitzer Science Center, 2006a), but none of them is directly applicable to our asteroid targets.

When observing a source with flux distribution $f(\lambda)$, the detector response per integration time, $R$, equals

$$R = f(\lambda_0) \int \frac{f(\lambda)}{f(\lambda_0)} \frac{R(\lambda)}{hc/\lambda} \mathrm{d}\lambda \tag{5.4}$$

**Table 5.5:** IRAC color-correction factors for NEATM asteroid spectra for several heliocentric distances $r$ (in AU), solar phase angles $\alpha$ (in degrees), model parameters $\eta$, and geometric albedos $p_V$ (the slope parameter $G$ is assumed to equal 0.15). The last column refers to the section in which the thus calculated color-correction factors are required.

| $r$ | $\alpha$ | $\eta$ | $p_V$ | Channel 1 | Ch. 2 | Ch. 3 | Ch. 4 | |
|---|---|---|---|---|---|---|---|---|
| 1.00 | 60.0 | 2.0 | 0.2 | 1.138 | 1.070 | 1.033 | 1.003 | Sect. 6.4 |
| 1.27 | 52.33 | 2.48 | 0.35 | 1.236 | 1.129 | 1.070 | 1.034 | Sect. 6.7 |

with the spectral detector response $R(\lambda)$ in units of electrons per photon (hence the division by the photon energy $hc/\lambda$; all integrals in this section run from 0 to $\infty$). The detector response to a target with spectrum $f_{tar}(\lambda)$, $R_{tar}$, and that to a calibration star with spectrum $f_{cal}(\lambda)$, $R_{cal}$, are then related to the monochromatic flux densities at the wavelength $\lambda_0$:

$$f_{tar}(\lambda_0) = f_{cal}(\lambda_0)\frac{R_{tar}}{R_{cal}} \times K \tag{5.5a}$$

$$K = \frac{f_{tar}(\lambda_0)}{f_{cal}(\lambda_0)}\frac{\int f_{cal}(\lambda)R(\lambda)/(hc/\lambda)\mathrm{d}\lambda}{\int f_{tar}(\lambda)R(\lambda)/(hc/\lambda)\mathrm{d}\lambda} \tag{5.5b}$$

with the *color-correction factor* $K$ taking account of the differences in spectral shape through the detector passband. Note in particular that $K$ is invariant under rescaling of both $f_{tar}$ and $f_{nom}$.

The IRAC BCD flux calibration includes a color correction assuming a nominal source spectrum $f_{nom}(\lambda) \propto \lambda^{-1}$. This requires a second color correction to be made:

$$f_{tar}(\lambda_0) = \frac{f_{nom}(\lambda_0)}{K} \tag{5.6a}$$

$$K = \frac{f_{nom}(\lambda_0)}{f_{tar}(\lambda_0)}\frac{\int f_{tar}(\lambda)R(\lambda)/(hc/\lambda)\mathrm{d}\lambda}{\int f_{nom}(\lambda)R(\lambda)/(hc/\lambda)\mathrm{d}\lambda}. \tag{5.6b}$$

We have developed a computer routine which calculates color correction factors for all IRAC channels and several model spectra, including NEATM asteroid spectra with variable model parameters. It makes use of the measured spectral response curves of each IRAC detector tabulated on-line by the SSC (`http://ssc.spitzer.caltech.edu/irac/spectral_response.html`). We have verified that our software reproduces all color correction factors quoted in the IRAC handbook (p. 48) to within one percent. See table 5.5 for IRAC color correction factors for NEATM spectra with several model parameters.

The values of $\lambda_0$ used in the IRAC BCD pipeline were chosen in a way that minimizes the dependence of color-correction factors on the spectral slope. They are defined the following way:

$$\lambda_0 = \frac{\int R(\lambda)\mathrm{d}\lambda}{\int R(\lambda)/\lambda\mathrm{d}\lambda}. \tag{5.7}$$

Evaluation of this integral for the four tabulated IRAC passbands yields effective wavelengths of 3.550, 4.493, 5.731, and 7.872 µm (see table 5.1 on p. 108).

#### 5.2.4.h Estimation of flux uncertainty

We estimated the statistical flux uncertainty in two mutually independent ways, which we added in quadrature:

- The standard statistical flux uncertainty derived from the scatter in the background flux level
- The scatter in the aperture-corrected fluxes derived using different possible radii for the synthetic aperture and the sky annulus (see sect. 5.2.4.f). This scatter is estimated to be a measure of the PSF deviation from its nominal form due to background structure or noise.

The accuracy of observations in channels 1–3 was generally limited by statistical uncertainty, while our highest signal-to-noise channel-4 observations were occasionally limited by the 3 % (Reach et al., 2005) calibration uncertainty.

On the basis of our data reduction pipeline validation experiments described in sect. 5.2.5 we estimate that our data reduction pipeline does not introduce major systematic uncertainties. We therefore neglect any systematic uncertainties resulting from, e.g., aperture correction (sect. 5.2.4.f) or color correction (sect. 5.2.4.g).

### 5.2.5 Validation of our data reduction pipeline

**Check against a calibration star** We have validated our data reduction pipeline by determining flux values which were known *a priori:* The brightness of a star used in the photometric calibration of IRAC. A list of such stars and their fluxes at IRAC wavelengths has been published by Reach et al. (2005). We have searched the database of publicly available Spitzer data and retrieved IRAC observations of the calibration standard star HD 165459 taken on 13 Feb 2006; the on-target

**Table 5.6:** Fluxes of the photometric calibration standard star HD 165459 from IRAC observations on 13 February 2006 (upper row) and expected values (lower row, quoted from Reach et al., 2005, Table 6). Values in the upper row are *not* color-corrected to enable comparison with the Reach et al. values. Uncertainties in the first row are statistical (from the synthetic aperture procedure), those in the second row are systematic (uncertainties in stellar flux modeling).

| | Channel 1 (mJy) | Channel 2 (mJy) | Channel 3 (mJy) | Channel 4 (mJy) |
|---|---|---|---|---|
| Determined | $643.9 \pm 4.1$ | $410.2 \pm 7.3$ | $264.3 \pm 8.2$ | $147.0 \pm 2.6$ |
| Expected | $647 \pm 17$ | $421 \pm 11$ | $268.7 \pm 7.1$ | $148.1 \pm 3.9$ |

integration time per FOV was 5 dither positions times 2 s. These observations were performed as part of a regular IRAC calibration program; the downloaded data were processed through the standard IRAC BCD pipeline.

We have determined flux values for the four IRAC channels using the method described in this section without color correction. As can be seen in table 5.6, fluxes agree with those given by Reach et al. (2005) within the error bars.

**Check pixel-scale effects** We use a mosaic pixel scale of $1.20''$, while a pixel scale of $\sim 1.22''$ is used for IRAC calibration. Note that the photometric calibration is tied to synthetic aperture photometry with an aperture of 10 pixels, so the pixel scale would be expected to matter.

In order to verify that this does not introduce an appreciable calibration uncertainty, we have mosaicked the above-mentioned HD 165459 data twice, using pixel scales of 1.20 and $1.22''$, respectively. Fluxes resulting from synthetic aperture photometry (with "default" radii of 10, 10, and 20 pixels) agree to within a few permille.

We have also determined aperture correction factors on the $1.22''$ pixel scale mosaics using the method described in sect. 5.2.4.f. As expected, the thus determined aperture correction factors differ significantly from those quoted in table 5.4 on p. 121, but match those tabulated in the IRAC datahandbook, p. 53, to within 1 %.

## 5.3 InfraRed Spectrograph (IRS)

The InfraRed Spectrograph (IRS; see Houck et al., 2004) covers the mid-wavelength range of Spitzer's spectral coverage with spectroscopic capabilities over the wave-

length range from 5.3 to 38 µm at two different spectral resolutions (referred to as low and high resolution in the following); and additional small-FOV imaging capabilities (peak-up imaging, PUI) at central wavelengths around 16 and 22 µm. At IRS wavelengths, asteroid flux is practically purely thermal.

After a short overview of the instrument over-all layout and its capabilities as used in our programs (sect. 5.3.1), we detail our observing strategies and data reduction techniques in section 5.3.2 and 5.3.3 for peak-up imaging and low-resolution spectroscopy, respectively. The high-resolution spectroscopy mode is not used in our programs and is generally disregarded in the following.

More information on the instrument can be found in Houck et al. (2004), the SOM, chapter 7, and in the IRS data handbook provided on-line (Spitzer Science Center, 2006b) (we made use of version 2.0 from 1 Apr. 2006, `http://ssc.spitzer.caltech.edu/irs/dh/`). A technical reference for the IRS BCD pipeline (see sect. 5.1.5) is the IRS pipeline description (Spitzer Science Center, 2005b).

### 5.3.1 Instrument layout

Similar to IRAC, IRS is composed of four detectors, located in the Cryogenic Telescope Assembly at a helium bath temperature of 1.4 K, and a set of control units located in the Spacecraft Bus at a higher temperature (see Fig. 5.2 on p. 102). The four blocked-impurity-band detectors have $128 \times 128$ pixels each, two detectors cover the IRS wavelength range at low spectral resolution ($\lambda/\Delta\lambda$ between 64 and 128) and two at high resolution around 600. The two short-wavelength detectors are Si:As arrays and referred to as Short-Low (SL) and Short-High (SH) for low and high spectral resolution, respectively. Analogously, the long-wavelength detectors, Si:Sb arrays, are referred to as Long-Low (LL) and Long-High (LH). The low-resolution modules use single diffraction gratings, the high-resolution modules employ a cross-dispersed echelle layout. Light from the two imaging apertures is projected onto two designated fields on the SL chip, with an effective FOV of $54'' \times 81''$ each at a pixel scale around $1.8''$ ($30 \times 45$ pixels). The focal plane apertures of the IRS modules have no overlap on the sky; bringing a target from one aperture to another requires slewing the spacecraft since IRS does not have any moving parts.

The spectroscopy modules employ narrow slit designs, where the slit width equals the point-spread function (PSF) width at the largest wavelength—due to diffraction-limited imaging the PSF width increases with wavelength. The pro-

jected slit widths are 3.6″ (SL), 4.7″ (SH), 10.5″ (LL), and 11.1″ (LH).

Ground-based tests showed the photometric response of the detectors to be temporally stable within 1 %. The absolute photometric accuracy of spectroscopic observations is typically limited by spill-over losses due to source mis-centering, which are reduced by a procedure called peak up (see below).

For science observations, the IRS detectors use a read-out system named "sample-up-the-ramp" whereby each pixel is read out non-destructively a number of times at the beginning of each measurement, and an equal number of times at the end of each measurement before the detector is reset. This reduces read-out noise and helps mitigate cosmic ray hits. It also enables meaningful data to be extracted from moderately saturated pixels, although at reduced signal-to-noise.

**Peak up** The $1\sigma$ accuracy of blind Spitzer pointings is 0.5″ (see sect. 5.1.2 on p. 103), therefore significant parts of the PSF are at risk of being placed outside the slit, in particular for the narrow short-wavelength slits. Mis-centering of spectroscopy targets results in systematic underestimation of the absolute flux level and furthermore introduces a spurious spectral slope over the sub-module's spectral range because the PSF broadens with wavelength, leading to larger losses.

IRS offers a mechanism, called *peak up,* to center spectroscopy targets in the slit more accurately, using more accurate small slews after refining spacecraft pointing on one of two dedicated imaging arrays called *peak-up arrays.*[4] The latter are also used for photometric imaging in the PUI mode which is discussed in sect. 5.3.2. Peaking up also enables spectroscopy of targets with relatively large positional uncertainty, which would otherwise be impossible to acquire.

Peak up zeroes in on the brightest source within a $24 \times 24$-pixel ($43.2'' \times 43.2''$) square centered at the nominal position of the peak-up target. The peak-up target can be the spectroscopy target itself or a near-by source whose position relative to the spectroscopy target is accurately known (see SOM, for details). The brightness of peak-up targets should be within 5–150 mJy at 16 µm or 15–340 mJy at 22 µm, depending on the peak-up array selected.

### 5.3.2 Peak-Up Imaging (PUI)

Although originally designed for peak up only, the two peak-up FOVs can be used to provide science-quality photometry. Since Spitzer cycle II (summer 2005), Peak-Up Imaging (PUI) is an IRS operation mode fully supported by the Spitzer

[4] There is a third peak-up option, which is however not available for moving targets (see SOM).

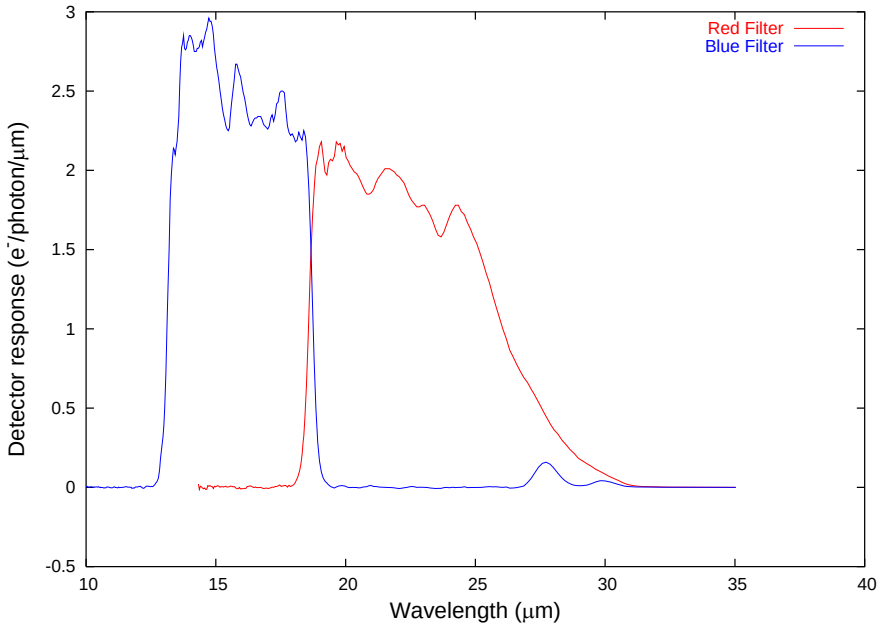


**Figure 5.7:** Detector response curves for the two IRS peak-up arrays. Depicted is the product of the total filter transmission and the spectral detector quantum efficiency, from the files linked at `http://ssc.spitzer.caltech.edu/irs/spectral_response.html`. Note the slight leak in the blue filter longward of 25 μm.

Science Center, which includes regular calibration observations and a dedicated BCD pipeline.

Light entering the two peak-up apertures is passed through suitable bandpass filters and then projected onto two designated parts of the SL detector, which are not used for spectroscopy. Both FOVs have a total size of $41 \times 56$ pixels with significant vignetting at the boundaries; the un-vignetted part in either FOV is $30 \times 45$ pixels corresponding to roughly $54'' \times 81''$ at a pixel scale around $1.8''$. After a PUI observation, the entire SL chip is read out, providing low-resolution spectra in two orders and imaging in both peak-up fields. Only one of the four fields-of-view, however, is on a given point-source target, the others observe neighboring "serendipitous" fields.

See Fig. 5.7 for detector response curves for the two PU arrays. The effective wavelength of the "blue" filter is around 16 μm, that of the "red" filter is about 22 μm, the FWHM spectral breadth of either is some 30 %.

**Table 5.7:** PUI point-source sensitivity ($1\sigma$ in units of µJy; see also eqn. 5.2 on p. 109) for one image frame of the stated integration time (frame time). The celestial background is assumed to be high, as is appropriate for most asteroid observations.

| Frame time (sec) | "Blue" filter (16 µm) | "Red" filter (22 µm) |
|---|---|---|
| 30 | 80 | 120 |
| 14 | 120 | 180 |
| 6 | 190 | 280 |

**Table 5.8:** Largest non-saturated point-source flux (in units of mJy) for the two PUI filters and high celestial background. Units in this table are mJy, *not* µJy as in table 5.7! Note that imaging of somewhat brighter sources is possible regardless of saturation, although at reduced signal-to-noise, due to the sample-up-the-ramp read-out mode (see sect. 5.3.1).

| Frame time (sec) | "Blue" filter (16 µm) | "Red" filter (22 µm) |
|---|---|---|
| 30 | 35 | 80 |
| 14 | 80 | 190 |
| 6 | 180 | 410 |

#### 5.3.2.a Instrument performance

Three values for the frame time, i.e. the integration time per frame, are selectable: 6, 14, and 30 s. See table 5.7 for the corresponding point-source sensitivities and table 5.8 for the saturation limits. As in the case of IRAC (see sect. 5.2.2), longer integrations can be achieved by repeating frames in-place or by dithering; this will be discussed in sect. 5.3.2.b. For deep PUI observations, the dominant source of uncertainty is celestial background radiation due to the thermal emission of zodiacal dust which is concentrated in the ecliptic plane. Most of our asteroid observations took place at low ecliptic latitudes, hence we assumed the most conservative sensitivity values ("high" background) for planning of observations. In the IRS datahandbook (Spitzer Science Center, 2006b, p. 50), systematic uncertainties in the PUI flux calibration are advertised to be within 6 % (see also sect. 5.3.2.e).

Similar to IRAC, PUI imaging suffers from a slight amount of optical distortion due to the instrument's offset from the telescope optical axis. While less severe than in the case of IRAC (see sect. 5.2.1) due to the smaller field-of-view, distortion must be accounted for in the data reduction to avoid significant photometric errors.

#### 5.3.2.b Asteroid observation strategies

The design of our PUI observations was similar to that of our IRAC observations (see sect. 5.2.2)—note that all our PUI targets were also observed with IRAC.

Required integration times were estimated on the basis of the sensitivities given in table 5.7 and lower limits on expected target flux (see also sect. 5.2.2.a); a typical flux uncertainty at PUI wavelengths is a factor 3. Identical timing constraints were imposed on IRAC and PUI observations of the respective asteroid targets, thus preventing bright IRAS sources from temporarily damaging the detector through latent effects (see sect. 5.2.2.b). We typically dithered (see sect. 5.2.2.c) around the nominal target positions (4 or more dither positions) to mitigate cosmic ray hits and defective pixels; note that due to the limited FOV size, PUI dithering distances are much smaller than for IRAC.

#### 5.3.2.c BCD pipeline

As for all Spitzer science data, PUI data are partially reduced and calibrated at the Spitzer Science Center (SSC) using an automated set of computer routines called the PUI BCD pipeline (see sect. 5.1.5). The PUI BCD pipeline is *mutatis mutandis* nearly identical to the IRAC BCD pipeline (see sect. 5.2.3), we here sketch the former, focusing on differences among the two. One BCD file per filter and pointing is produced, i.e. a FITS file with most known instrument artefacts removed and in physical flux units (MJy/sr). Each BCD file is associated with several ancillary files including maps of estimated flux uncertainty and masks where potentially unreliable pixels are flagged (e.g. suspected cosmic ray hits, vignetted pixels, and permanently damaged pixels); those ancillary files are useful for further data reduction. Technical references for the PUI BCD pipeline are the IRS pipeline description (Spitzer Science Center, 2005b) and the IRS datahandbook (Spitzer Science Center, 2006b).

Corrections for dark current are determined as in the case of IRAC (see sect. 5.2.3.a), but no time-dependent drift has been found, i.e. there is no first-frame effect (see sect. 5.2.3.b). PUI data are flat-fielded similar to IRAC data (see sect. 5.2.3.c) and flux calibrated against a set of stellar calibrators (see sect. 5.2.3.d and SOM, p. 178; flux calibration will be further discussed in sect. 5.3.2.e). As in the case of IRAC, PUI data are flux calibrated assuming a target spectrum inversely proportional to wavelength, necessitating color corrections to be made (see sect. 5.3.2.d). Pointing refinement, as is done for IRAC data (see sect. 5.2.3.e), is not

performed on PUI data; it would not be feasible in general due to the low density of bright stars at PUI wavelengths.

All IRS detectors including the SL chip used for PUI are subject to the damaging effects of solar flares, resulting in an increasing number of permanently or temporarily defective pixels. As a part of calibration activities, the SSC monitors the pixel responsivity and flags permanently damaged pixels as "dead" in the BCD pipeline. Some pixels, called "rogue pixels," are overly responsive at times, but operate normally most of the time. The SSC issues regularly updated lists of rogue pixels, but rogue pixels are not flagged in BCD files.

#### 5.3.2.d Data-reduction steps taken by us

Reduction of PUI data is largely analogous to IRAC data reduction (see sect. 5.2.4). The most significant differences are the following:

**Visual inspection** While all PUI data frames were visually inspected, no unusable PUI frames were found. This is due to the much lower density of bright stars at PUI wavelengths relative to IRAC wavelengths, but also due to the sample-up-the-ramp read-out mode (see sect. 5.3.1) mitigating the effects of cosmic-ray hits. Rogue pixels (see sect. 5.3.2.c), however, are clearly recognizable as such in visual inspection. It turned out to be easier to manually add them to the bad-pixel map provided by the BCD pipeline than to tweak the mosaic routines (see below) to reliably recognize rogue pixels without falsely flagging good pixels. To lighten this task, an IDL routine was developed which flags a rogue pixel for all BCDs belonging to a series of consecutive observations.

**Background matching** Since no first-frame effect is present, background matching (see sect. 5.2.4.b) is not needed.

**Mosaicking** A mosaic pixel scale of $1.8''$ is used. Generally, no cosmic-ray hits or background sources are present in BCD images. Rogue pixels were rejected manually (see above). It is important to have *mosaic.pl* disregard pixels in the vignetted region close to the FOV boundary, where no reliable flat fielding is possible. They are flagged as vignetted in the BCD-provided bad-pixel map but not rejected by default.

**Table 5.9:** Aperture correction factors $AC_{i,j,k}$ (see eqn. 5.3 on p. 120) for the two PUI filters and different aperture radii (in mosaic pixels of 1.8″ each). Inner and outer sky annulus radii are 8 and 14 pixels, respectively. (from Spitzer Science Center, 2006b, p. 50)

| Aperture | Blue filter | Red filter |
|---|---|---|
| 2 | 1.69 | 2.13 |
| 3 | 1.38 | 1.57 |
| 4 | 1.16 | 1.36 |
| 5 | 1.07 | 1.18 |
| 6 | 1.05 | 1.07 |
| 7 | 1.04 | 1.03 |
| 8 | 1.03 | 1.02 |
| 9 | 1.02 | 1.02 |
| 10 | 1.01 | 1.01 |
| 11 | 1.00 | 1.01 |
| 12 | 1.00 | 1.01 |

**Table 5.10:** IRS PUI color-correction factors for NEATM asteroid spectra for several heliocentric distances $r$ (in AU), solar phase angles $\alpha$ (in degrees), model parameters $\eta$, and geometric albedos $p_V$ (the slope parameter $G$ is assumed to equal 0.15). The last column refers to the section in which the thus calculated color-correction factors are required. The effective wavelengths were calculated from eqn. 5.7 on p. 123.

| $r$ | $\alpha$ | $\eta$ | $p_V$ | Blue (15.8 µm) | Red (22.3 µm) | |
|---|---|---|---|---|---|---|
| 1.00 | 60.0 | 2.0 | 0.2 | 0.982 | 0.994 | Sect. 6.4 |

**Flux extraction, aperture correction, color correction** The PUI flux calibration is based on synthetic aperture photometry using a sky annulus with inner and outer radii of 8 and 14 pixels, respectively, and aperture radii of 3 (blue) and 4 (red) pixels (Spitzer Science Center, 2006b).[5] These aperture radii are small compared to the FWHM width of the PSF, which is around 2 (blue) and 2.5 (red) pixels, hence fluxes are aperture corrected by default. We generally used larger aperture radii and the quoted sky annulus radii; see table 5.9 for aperture correction factors. See table 5.10 for color-correction factors which were determined like their IRAC counterparts (see table 5.5 on p. 122) but using the PUI detector response (see Fig. 5.7 on p. 127).

[5] These values appear to have changed with the new BCD pipeline version 15—see sect. 5.3.2.e.

**Table 5.11:** Determined fluxes of the star HD 163466, which was used for PUI flux calibration, from PUI observations on 20 Apr, 26 Apr, and 26 May 2006. Fluxes should be (Spitzer helpdesk, private email communication from 24 Feb 2006): 54.29 mJy (blue) and 27.44 mJy (red) before color correction.

| Date | "blue" flux (mJy) | off by (%) | "red" flux (mJy) | off by (%) |
|---|---|---|---|---|
| 2006/04/20 | $51.06 \pm 0.30$ | -5.9 | $28.61 \pm 0.16$ | +4.3 |
| 2006/04/26 | $50.98 \pm 0.41$ | -6.1 | $28.86 \pm 0.13$ | +5.2 |
| 2006/05/26 | $51.57 \pm 0.47$ | -5.0 | $28.95 \pm 0.17$ | +5.5 |

#### 5.3.2.e Validation

We aimed at validating our PUI data reduction pipeline, like we have validated our IRAC pipeline (see sect. 5.2.5). However, as of April 2007, the Spitzer Science Center has not announced which flux standards were used for PUI flux calibration. Upon request, the Spitzer helpdesk informed us (private email communication from 24 Feb 2006) that the primary flux standard used for PUI calibration was the star HD 163466, with PUI fluxes of 54.29 mJy (blue) and 27.44 mJy (red) before color correction (similar to the IRAC calibration standard quoted in sect. 5.2.5).

PUI observations of that star were performed on 20 Apr, 26 Apr, and 26 May 2006 during regular IRS calibration observations, data are public. BCD files from these three observations were reduced by us using the data reduction pipeline described herein. The resulting flux values and their deviations from the nominal values are given in table 5.11.

We see significant deviations from the nominal values, roughly -5.5 % in the blue filter and roughly +5 % in the red filter. We have reported this discrepancy to the Spitzer helpdesk over summer and fall 2006. The helpdesk found no flaw in our data reduction pipeline but stated that our deviation in photometric zeropoints was well within the quoted uncertainty of ±6 %. We feel, however, that our results reveal a rather serious calibration issue with the BCD pipeline 14, possibly related to the fact that flux calibration is tied to synthetic aperture photometry with very small radii, leading to relatively large uncertainties due to the needed aperture correction.

It should also be noted that in PUI observations of an exoplanet, repeated over a timespan of 6 h, Deming et al. (2006) found a time dependent drift in PUI photometric gain, which cannot be explained to date.

**Update: pipeline version 15** The validation attempt presented in this section is based on the IRS BCD pipeline version 14, issued in Jul 2006. The Spitzer Science Center has issued an updated IRS BCD pipeline, version 15, on 28 Feb 2007 "which results in changes in measured photometric values of $< 15$ %."[6] All PUI data in the archive (including ours) have been reprocessed; however, at the time of writing, no updated pipeline documentation is available. We hope that this new pipeline version fixes the issues found herein and we will reprocess all our PUI data based on the reprocessed BCDs. *All PUI fluxes quoted in this thesis are therefore preliminary—updated PUI fluxes based on the IRS BCD pipeline version 15 will be used for journal publication.*

### 5.3.3 Low-resolution spectroscopy

Two modules (named SL and LL) provide low-resolution spectroscopy at a relative spectral resolution between 64 and 128 at wavelengths between 5.2 and 38.0 µm. Each module has two sub-apertures in its slit, bringing source light in 1st and 2nd diffraction order of its diffraction grating onto the respective chip. The two diffraction orders do not overlap on the chip (this is prevented using suitable bandpass filters in the optical path) nor on the sky. The telescope must be slewed in order to bring an observational target from one sub-slit into another. In total, four telescope pointings are required to observe a spectrum over the full low-resolution wavelength range, one per sub-slit. The projected slit widths of the two modules match the FWHM PSF widths at the largest wavelengths (Spitzer imaging is diffraction limited, hence the PSF width grows with wavelength). Their length is much larger, such that one-dimensional spatial resolution is acquired along the slit in addition to the spectral dimension. There is some spectral overlap among spectrally adjacent IRS modules and spectral orders, allowing spectra to be cross-checked. See table 5.12 for an overview of slit dimensions and spectral ranges.

IRS spectroscopy observations are specified in SPOT. Adjustable parameters are:

- Peak-up method and parameters (see sect. 5.3.1)
- Sub-modules to be used; if more than one module is selected, observations are ordered by wavelength with short wavelengths first, i.e. SL2, SL1, LL2,

[6] C.f. `http://ssc.spitzer.caltech.edu/archanaly/plhistory/irs.html`.

**Table 5.12:** IRS low-resolution modules: Overview of spectral coverage, detector pixel scale, and projected slit dimensions. Note the slight spectral overlap between the sub modules. PUI is performed on the SL detector.

| | Wavelength range | Pixel scale | Slit width | Slit length |
|---|---|---|---|---|
| SL 2nd order | 5.2–8.7 µm | 1.8″ | 3.6″ | 57″ |
| SL 1st order | 7.4–14.5 µm | 1.8″ | 3.7″ | 57″ |
| LL 2nd order | 14.0–21.7 µm | 5.1″ | 10.5″ | 168″ |
| LL 1st order | 19.5–38.0 µm | 5.1″ | 10.7″ | 168″ |

LL1 if all four low-resolution modules are selected[7]

- Integration time per frame and sub-module, where possible choices are 6, 14, 60, and 240 s for the SL modules; 6, 14, 30, and 120 s for the LL modules
- Number of frames ("cycles") to be taken at each position to increase the total integration time

There are two different spectroscopy modes: *staring* and *mapping*. Staring mode is primarily designed for point sources after successful peak up; in each sub-module the source is first placed at 33 % of the slit length, then at 66 %, at each position the specified number of frames is taken—the total integration time is thus twice the number of cycles times the frame time. The purpose of this "nodding" strategy is to enable correction for diffuse background emission. In mapping mode, the source is placed at a selectable number of offsets parallel and/or perpendicular to the slit direction, where the angular offset distances are adjustable. The mapping mode was designed for spectral maps of extended sources, but is also useful for spectroscopy of sources which cannot be peaked up on (see sect. 6.8).

**Instrument performance** See Fig. 5.8 for an overview of the sensitivities of the IRS low-resolution modules; the total signal-to-noise of an observation consisting of a series of $n$ frames is $\sqrt{n} \times f/s$ with flux $f$ and sensitivity $s$, provided other noise sources (e.g. shot noise) can be neglected. The maximum unsaturated flux is typically a few thousand times larger.

Laboratory tests on ground showed the temporal stability of the photometric response to an accurately centered source to be better than 1 %; in flight, the photometric stability is limited by source mis-centering. The overall absolute

[7] Pointing and tracking accuracy decays with time; this has a more profound influence on short-wavelength observations using relatively narrow slits.

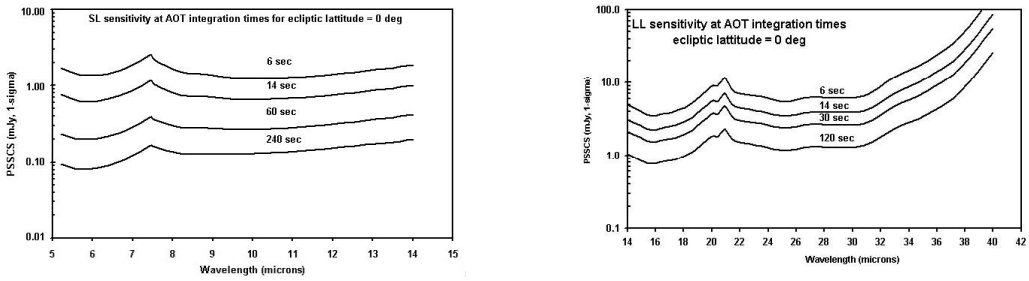


**Figure 5.8:** $1\sigma$ point-source sensitivity per frame for the SL (left) and LL (right) modules for the four possible frame times assuming low ecliptic latitude, i.e. high background due to zodiacal emission, as is appropriate for most asteroid observations. (Figs. from SOM, p. 160 and 161)

**Table 5.13:** Absolute photometric uncertainties due to spill-over losses for the SL and LL modules and the three selectable peak-up options. Note that the position uncertainty after a "low"-accuracy peak-up is actually worse than Spitzer's nominal pointing accuracy; it should only be used on sources of poorly known position. (see SOM, p. 187)

| | High | Moderate | Low |
|---|---|---|---|
| $1\sigma$ radial position uncertainty | $0.4''$ | $1.0''$ | $2.0''$ |
| Photometric uncertainty (SL) | 15–20 % | 37–42 % | $\sim$ 100 % |
| Photometric uncertainty (LL) | 2–5 % | 5–10 % | 15–20 % |

photometric uncertainty of IRS is around 10 %, dominated by uncertainty in stellar flux models (SOM, p. 210). See table 5.13 for an overview of photometric uncertainties due to spill-over losses.